

Supporting Information

High-Efficiency Co/Co_xS_y@S,N-Codoped Porous Carbon Electrocatalysts Fabricated from Controllably Grown Sulfur- and Nitrogen-Including Cobalt-Based MOFs for Rechargeable Zinc-Air Batteries

Shengwen Liu,^{†,‡} Xian Zhang,^{†,§,‡} Guozhong Wang,[†] Yunxia Zhang,[†] and Haimin

Zhang^{*,†}

[†] Key Laboratory of Materials Physics, Centre for Environmental and Energy Nanomaterials, Anhui Key Laboratory of Nanomaterials and Nanotechnology, Institute of Solid State Physics, Chinese Academy of Sciences, Hefei 230031, China

[§] University of Science and Technology of China, Hefei 230026, China

[‡] These authors contributed equally

Corresponding Author

*E-mail: zhanghm@issp.ac.cn;

Table S1. Surface area and total pore volume of Co-MOFs derived carbon products.

Samples	S_{BET}	V_{tol}
	$\text{m}^2 \text{g}^{-1}$	$\text{cm}^3 \text{g}^{-1}$
Co/Co _x S _y @SNCB-800	61.4	0.178
Co/Co _x S _y @SNCS-800	88.09	0.334
Co/Co _x S _y @SNCF-800	212.05	0.644
Co/Co _x S _y @SNCN-800	154.32	0.297

S_{BET} : surface area calculated from the nitrogen adsorption curve based on the BET model. V_{tol} : total pore volume calculated by DFT method.

Table S2. Elemental composition analysis of Co-MOFs derived carbon products by XPS measurement.

Samples	S 2p	C 1s	N 1s	O 1s	Co 2p	Co:S
Co/Co _x S _y @SNCB-800	5.40	61.04	3.11	27.15	3.29	0.61
Co/Co _x S _y @SNCS-800	5.45	62.26	2.48	20.69	9.11	1.67
Co/Co _x S _y @SNCN-800	5.07	84.01	3.25	5.66	2.01	0.40
Co/Co _x S _y @SNCF-800	5.32	61.28	2.80	26.6	4.00	0.75
Co/Co _x S _y @SNCF-900	3.68	69.01	2.31	21.95	3.06	0.83
Co/Co _x S _y @SNCF-700	3.80	50.99	2.86	30.49	11.85	3.12

Table S3. N doped type and content of Co-MOFs derived carbon products by XPS measurement.

Samples	Oxidized N	Pyridinic N	Graphitic N	Pyrrolic N
			(%)	
Co/Co _x S _y @SNCS-800	32.5	23.3	28.6	15.6
Co/Co _x S _y @SNCB-800	36.7	23.8	28.3	11.2
Co/Co _x S _y @SNCN-800	13.2	27.3	30.6	28.9
Co/Co _x S _y @SNCF-800	16.8	32.8	34.9	15.5
Co/Co _x S _y @SNCF-900	18.8	26.2	38.3	16.7
Co/Co _x S _y @SNCF-700	21.2	43.6	18.0	17.2

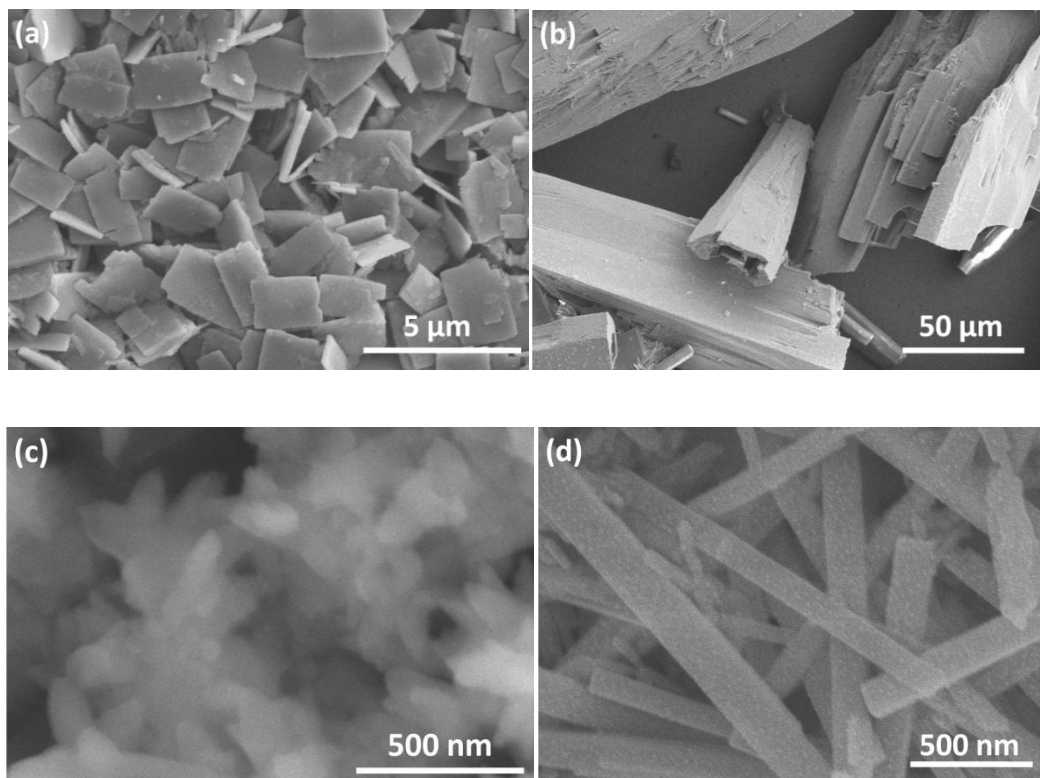


Figure S1. High magnification SEM images of as-prepared $[\text{Co}(\text{Tdc})(\text{Bpy})]_n$ MOFs. (a) 2D sheets obtained in $\text{H}_2\text{O}/\text{NaOH}$ at room temperature; (b) 3D bulks obtained in $\text{H}_2\text{O}/\text{NaOH}$ under hydrothermal conditions; (c) 1D nanorods obtained in MeOH/NaOH at room temperature; (d) 2D fibers in MeOH/NaOH under hydrothermal conditions.

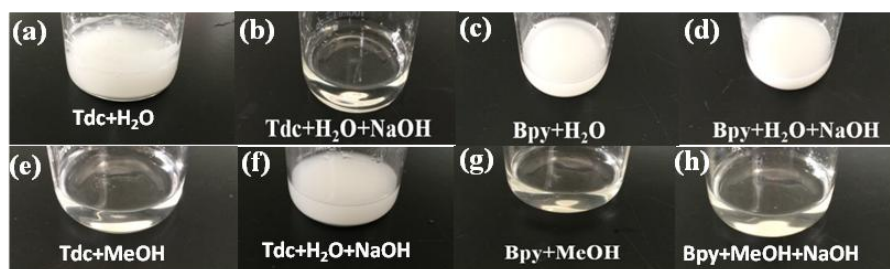


Figure S2. Optical photos of initial Co^{2+} -containing reaction solutions. (a), (b) Tdc+ H_2O and Tdc+ H_2O +NaOH; (c), (d) Bpy+ H_2O and Bpy+ H_2O +NaOH; (e), (f) Tdc+MeOH and Tdc+MeOH+NaOH; (g), (h) Bpy+MeOH and Bpy+MeOH+NaOH.

Figure S2 shows the optical photos of initial Co^{2+} -containing $\text{H}_2\text{O}/\text{NaOH}$ and MeOH/NaOH reaction solutions at room temperature. Obviously, $\text{H}_2\text{O}/\text{NaOH}$ system can facilitate the dissolution of Tdc (Figure S2a, b) owing to a high efficient deprotonation of Tdc at the presence of NaOH, while only slight dissolution of Bpy can be observed in such system (Figure S2c, d) primarily due to the nonpolar property of Bpy (H_2O polarity of 10.2). The opposite results can be obtained in MeOH/NaOH system at room temperature (Figure S2e-h). Actually, Tdc and Bpy should have high solubility in MeOH (the polarity of 6.6) ascribed to their nonpolar properties. However, the deprotonated Tdc by introduction of NaOH exhibits very low dissolution in MeOH/NaOH (Figure S2f). In $\text{H}_2\text{O}/\text{NaOH}$ system, a high solubility of Tdc accompanying with a slight dissolution of Bpy should be very beneficial for the growth of 2D Co-Tdc sheets with less Bpy pillared layers at room temperature, whereas a low solubility of Tdc in MeOH/NaOH system accompanying with a high dissolution of Bpy is unfavourable for the growth of 2D Co-Tdc sheets, tending to the formation of Co-MOFs along 1D direction with more Bpy pillared layers at room temperature. On basis of the formed Co-MOFs structure units in two reaction systems at room temperature, a hydrothermal treatment can effectively facilitate the dissolution of Bpy in $\text{H}_2\text{O}/\text{NaOH}$ and Tdc in MeOH/NaOH , thus leading to a further growth of Co-MOFs structures. The above speculation has been verified by the obtained Co-MOFs morphology information in different reaction systems (Figure 1 and Figure S1).

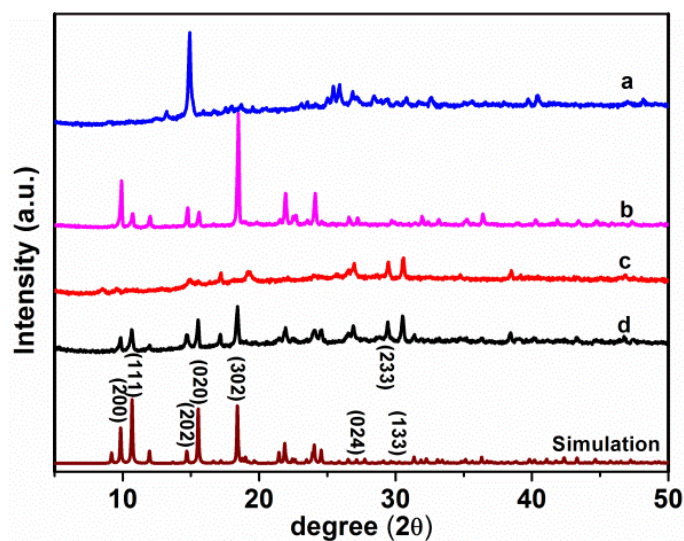


Figure S3. XRD patterns of as-prepared Co-MOFs samples at different conditions. Lines a and c of 2D sheets obtained in $\text{H}_2\text{O}/\text{NaOH}$ and 1D nanorods obtained in MeOH/NaOH at room temperature; Lines b and d of 3D bulks obtained in $\text{H}_2\text{O}/\text{NaOH}$ and 1D fibers obtained in MeOH/NaOH under hydrothermal conditions.

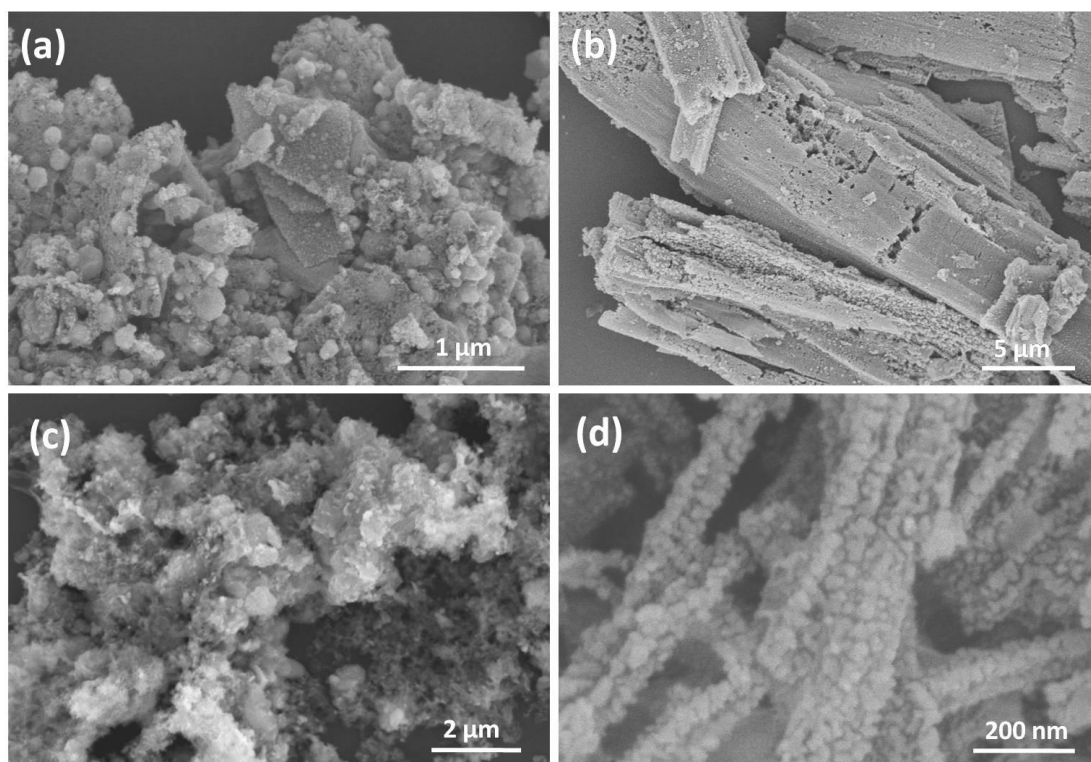


Figure S4. SEM images of Co-MOFs derived carbon-based products. (a) Co/Co_xS_y@SNCS-800; (b) Co/Co_xS_y@SNCB-800; (c) Co/Co_xS_y@SNCN-800; (d) Co/Co_xS_y@SNCF-800.

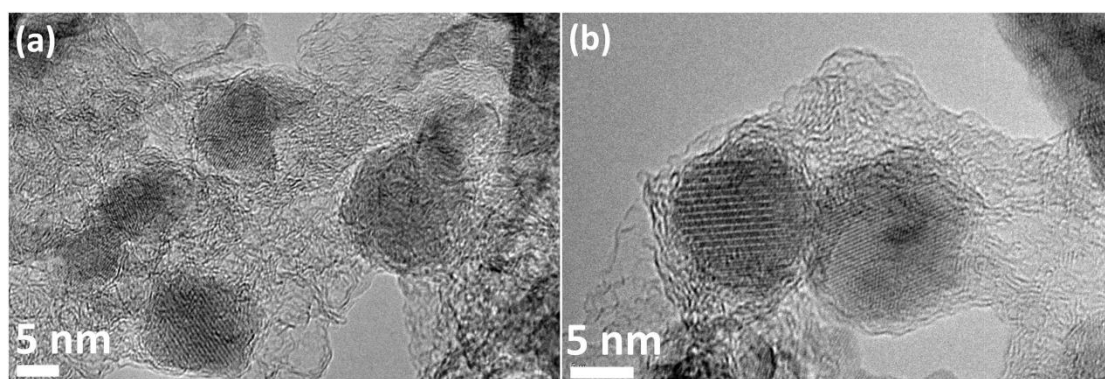


Figure S5. TEM images (a, b) of Co/Co_xS_y@SNCF-800 obtained from different locations.

Apparently, the formed Co/Co_xS_y nanoparticles are encapsulated into graphitic carbon structure, which is very beneficial for improving the materials' stability during electrocatalysis.

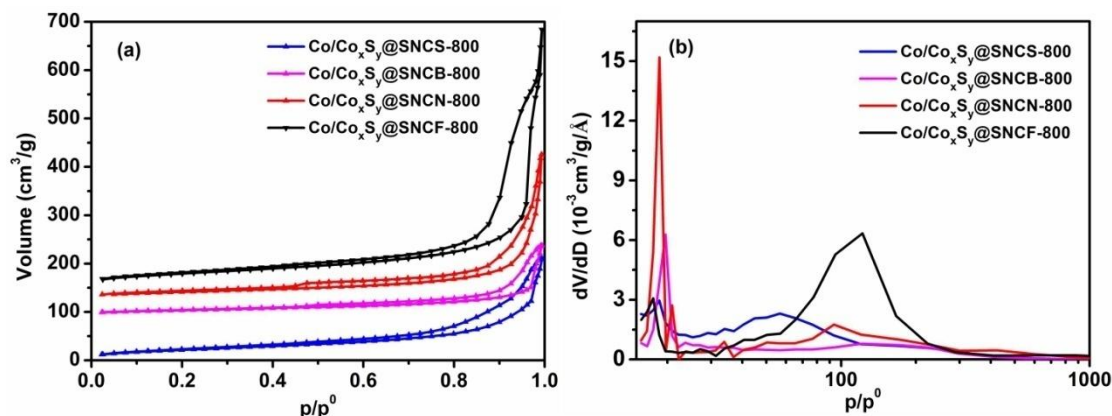


Figure S6. (a) N₂ adsorption-desorption isotherms of Co/Co_xS_y@SNCS-800, Co/Co_xS_y@SNCB-800, Co/Co_xS_y@SNCN-800 and Co/Co_xS_y@SNCF-800; (b) The corresponding pore size distribution curves.

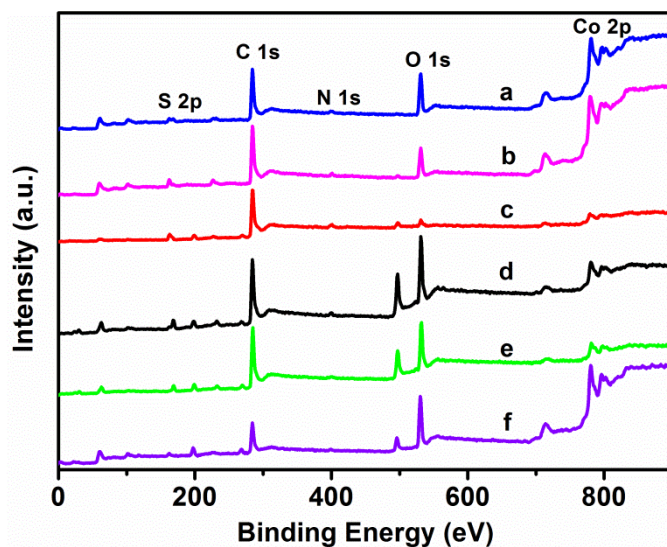


Figure S7. XPS survey spectra of the Co-MOFs derived carbon materials. Lines a, b, c, d, e and f are Co/Co_xS_y@SNCS-800, Co/Co_xS_y@SNCB-800, Co/Co_xS_y@SNCN-800, Co/Co_xS_y@SNCF-800, Co/Co_xS_y@SNCF-900 and Co/Co_xS_y@SNCF-700, respectively.

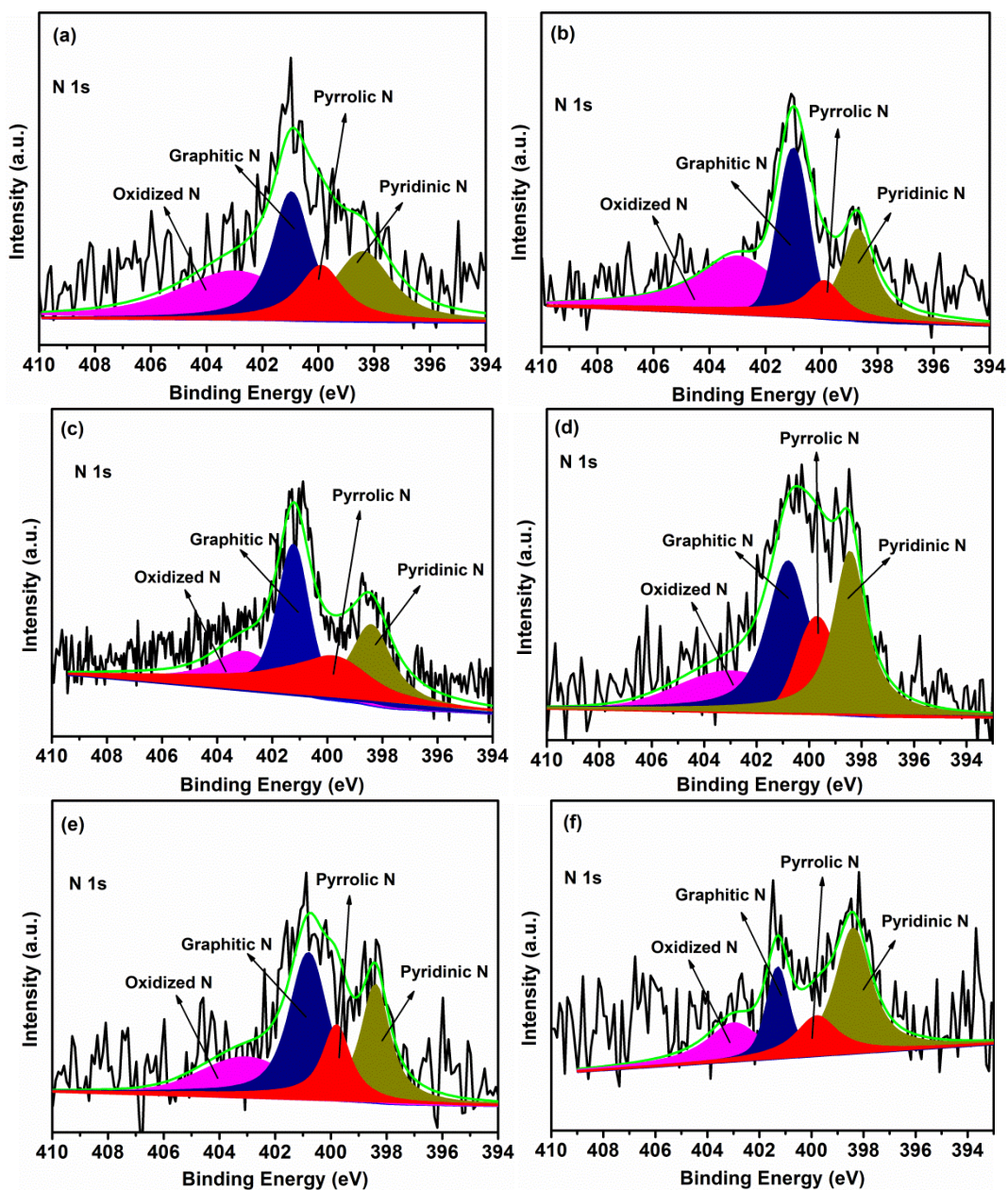


Figure S8. High resolution N 1s XPS spectra of (a) Co/Co_xS_y@SNCS-800; (b) Co/Co_xS_y@SNCB-800; (c) Co/Co_xS_y@SNCS-800; (d) Co/Co_xS_y@SNCF-800; (e) Co/Co_xS_y@SNCF-900; (f) Co/Co_xS_y@SNCF-700.

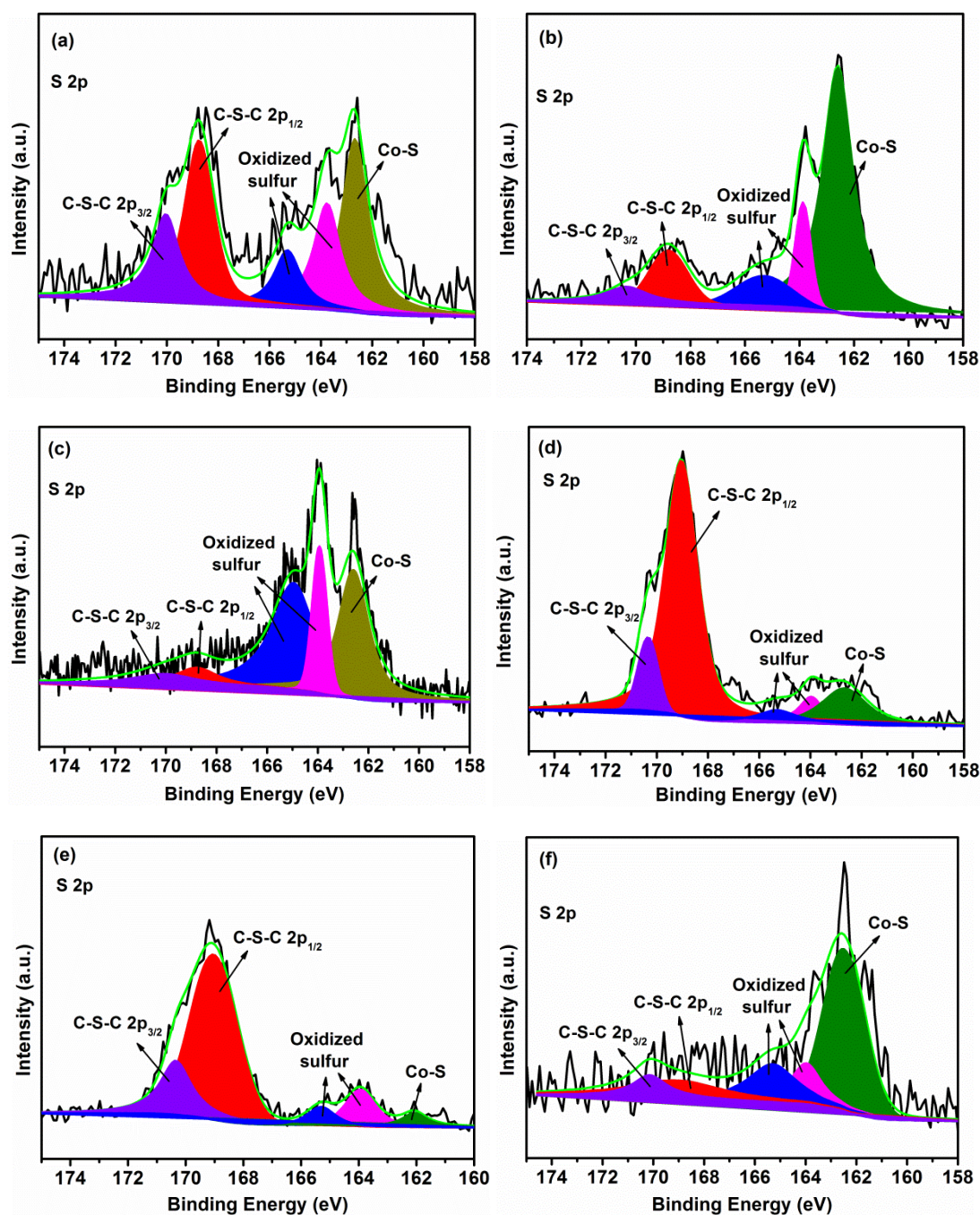


Figure S9. High resolution S 2p XPS spectra of (a) Co/Co_xS_y@SNCS-800; (b) Co/Co_xS_y@SNCB-800; (c) Co/Co_xS_y@SNCN-800; (d) Co/Co_xS_y@SNCF-800; (e) Co/Co_xS_y@SNCF-900; (f) Co/Co_xS_y@SNCF-700.

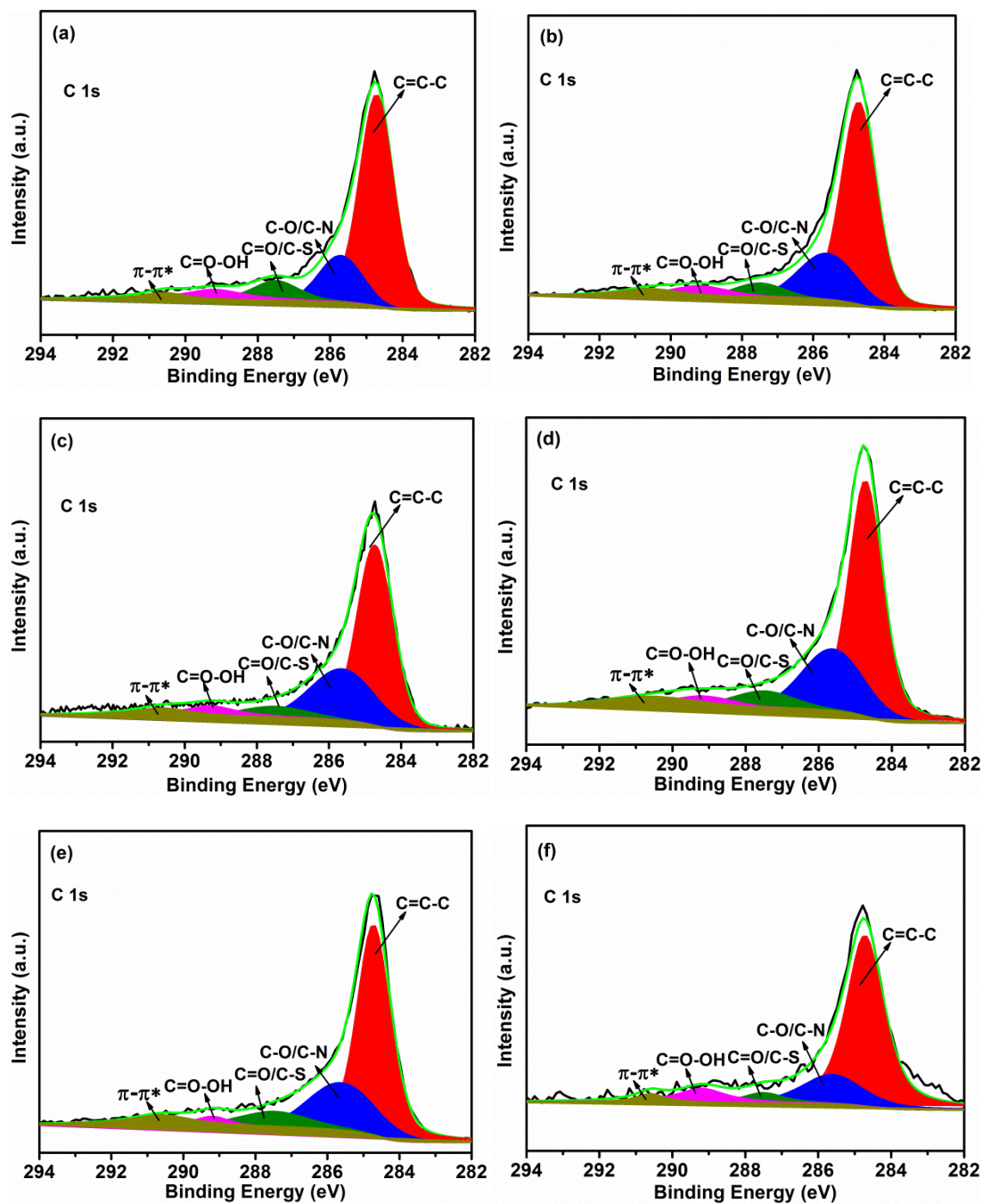


Figure S10. High resolution C 1s XPS spectra of (a) Co/Co_xS_y@SNCS-800; (b) Co/Co_xS_y@SNCB-800; (c) Co/Co_xS_y@SNCN-800; (d) Co/Co_xS_y@SNCF-800; (e) Co/Co_xS_y@SNCF-900; (f) Co/Co_xS_y@SNCF-700.

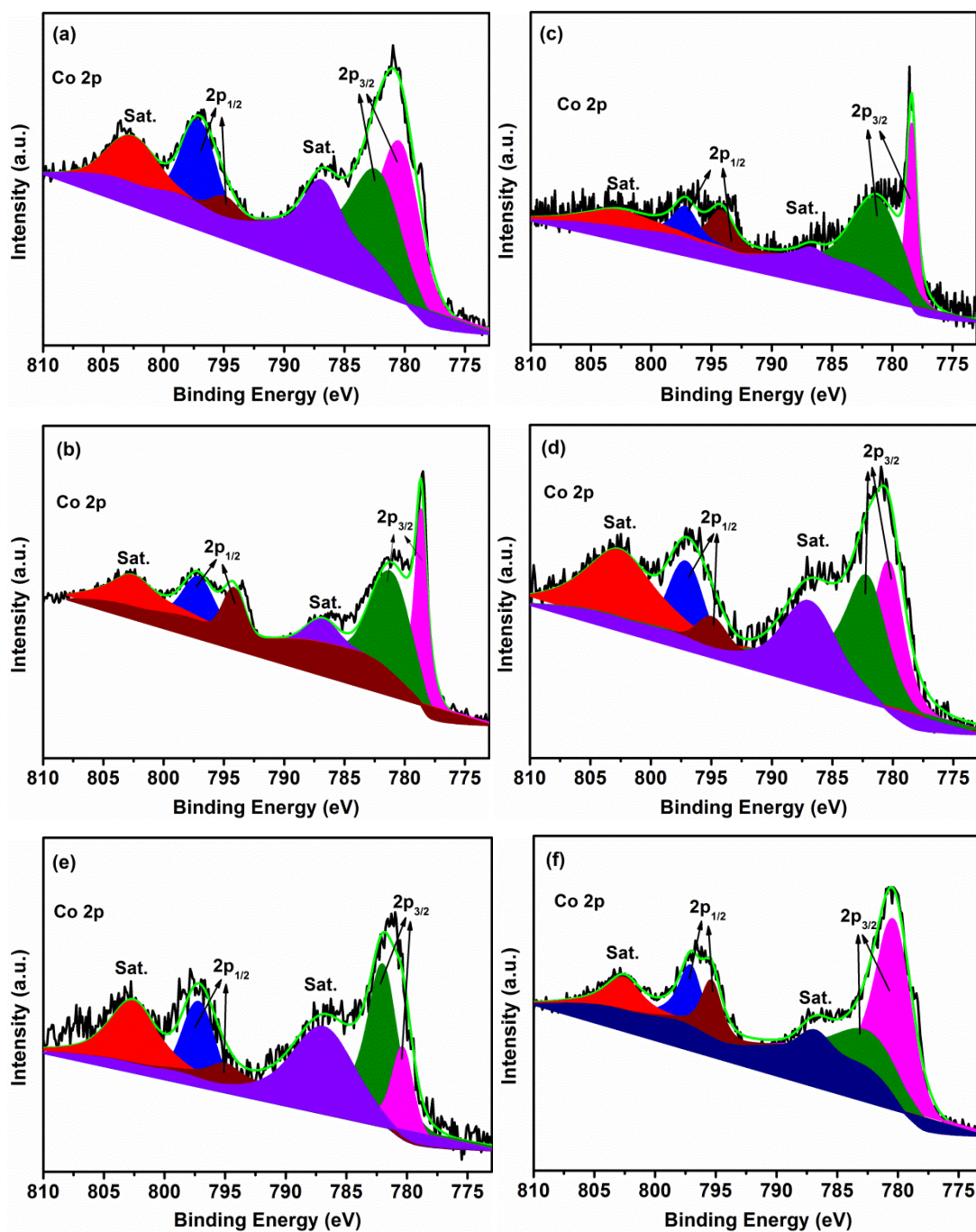


Figure S11. High resolution Co 2p XPS spectra of (a) Co/Co_xS_y@SNCS-800; (b) Co/Co_xS_y@SNCB-800; (c) Co/Co_xS_y@SNCN-800; (d) Co/Co_xS_y@SNCF-800; (e) Co/Co_xS_y@SNCF-900; (f) Co/Co_xS_y@SNCF-700.

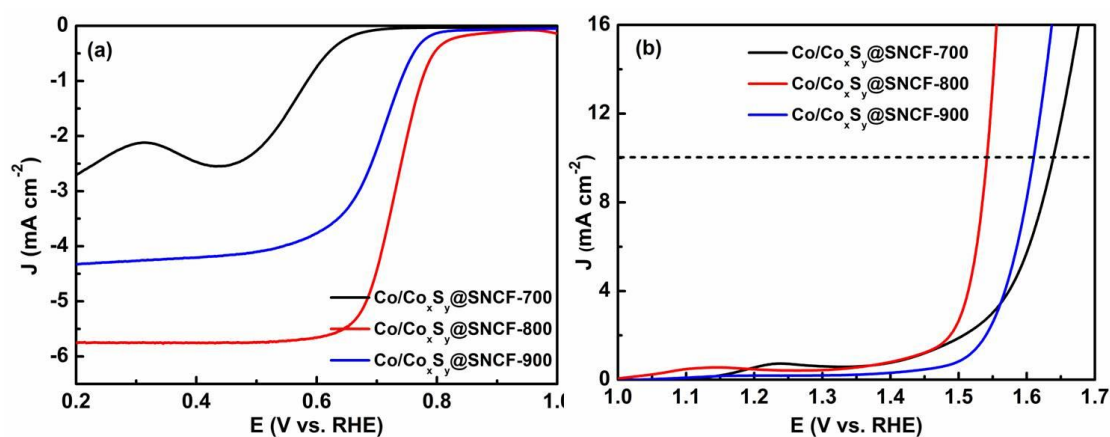


Figure S12. LSV curves of different electrocatalysts of Co/Co_xS_y@SNCF-700, Co/Co_xS_y@SNCF-800 and Co/Co_xS_y@SNCF-900 for (a) ORR and (b) OER measurements.

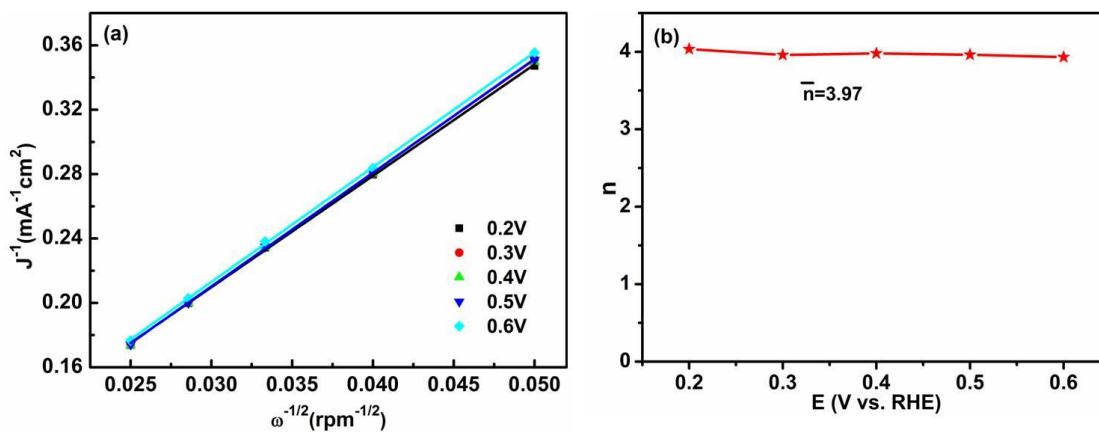


Figure S13. (a) LSV curves of Co/Co_xS_y@SNCF-800 at various rotation rates; (b) Corresponding Koutecky–Levich plots derived from the RDE data; inset of electron transfer number of Co/Co_xS_y@SNCF-800 at 0.2 V~0.6 V.

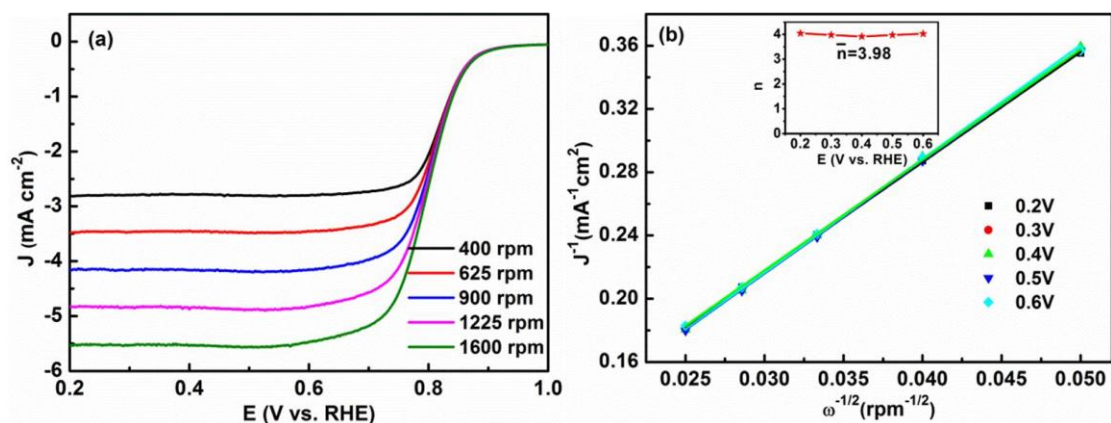


Figure S14. (a) LSV curves of Pt/C at various rotation rates; (b) Corresponding Koutecky–Levich plots derived from the RDE data; inset of electron transfer number of Pt/C catalyst at 0.2 V~0.6 V.

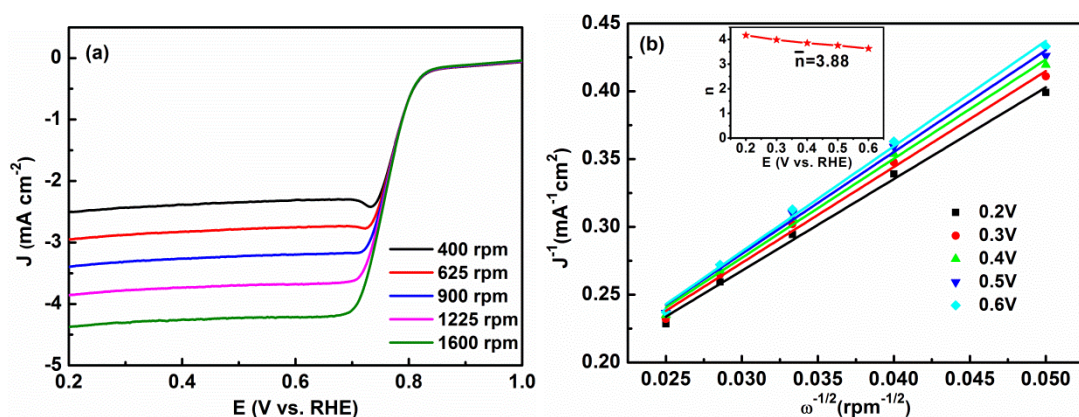


Figure S15. (a) LSV curves of Co/Co_xS_y@SNCS-800 at various rotation rates; (b) Corresponding Koutecky–Levich plots derived from the RDE data; inset of electron transfer number of Co/Co_xS_y@SNCS-800 at 0.2 V~0.6 V.

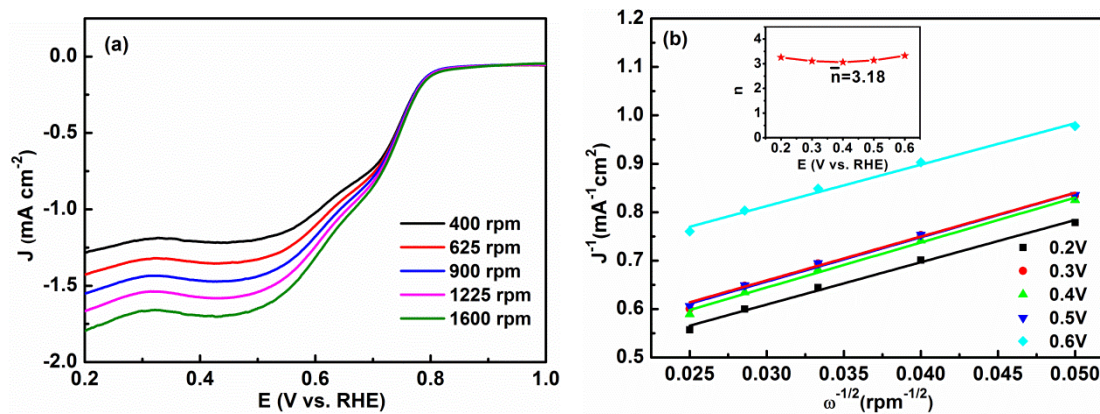


Figure S16. (a) LSV curves of Co/Co_xS_y@SNCB-800 at various rotation rates; (b) Corresponding Koutecky–Levich plots derived from the RDE data; inset of electron transfer number of Co/Co_xS_y@SNCS-800 at 0.2 V~0.6 V.

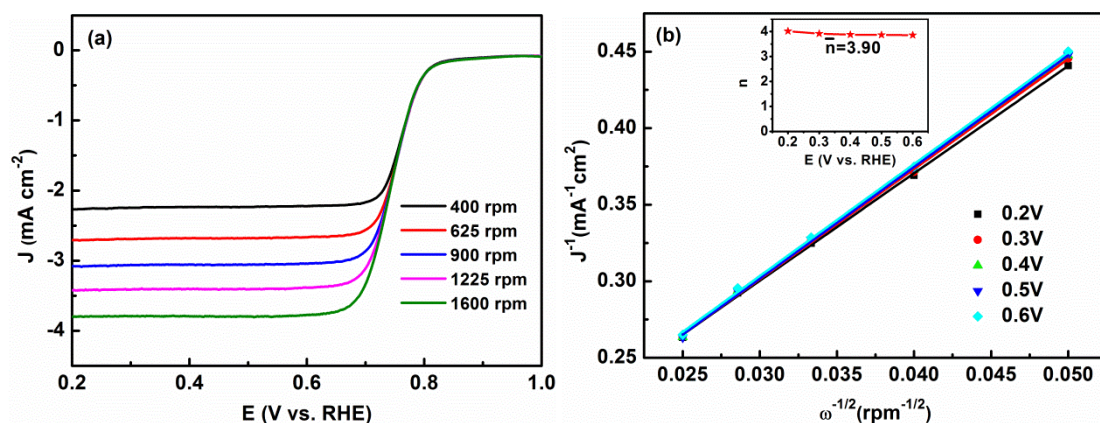


Figure S17. (a) LSV curves of Co/Co_xS_y@SNCN-800 at various rotation rates; (b) Corresponding Koutecky–Levich plots derived from the RDE data; inset of electron transfer number of Co/Co_xS_y@SNCN-800 at 0.2 V~0.6 V.

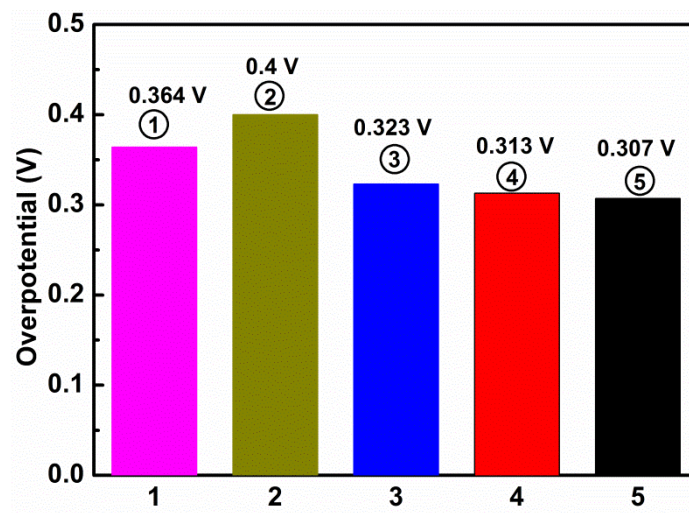


Figure S18. The overpotentials at current density of 10 mA cm^{-2} of all investigated electrocatalysts at 1600 rpm at a scan rate of 10 mV s^{-1} in O_2 -saturated 0.1 M KOH solution. ① Co/Co_xS_y@SNCS-800, ② Co/Co_xS_y@SNCB-800, ③ Co/Co_xS_y@SNCN-800, ④ Co/Co_xS_y@SNCF-800, ⑤ RuO₂.

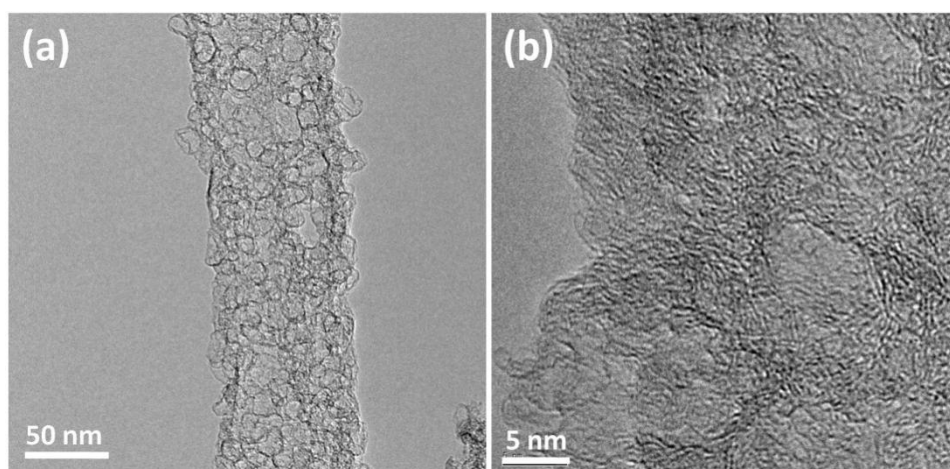


Figure S19. TEM images (a, b) of SNCF-800

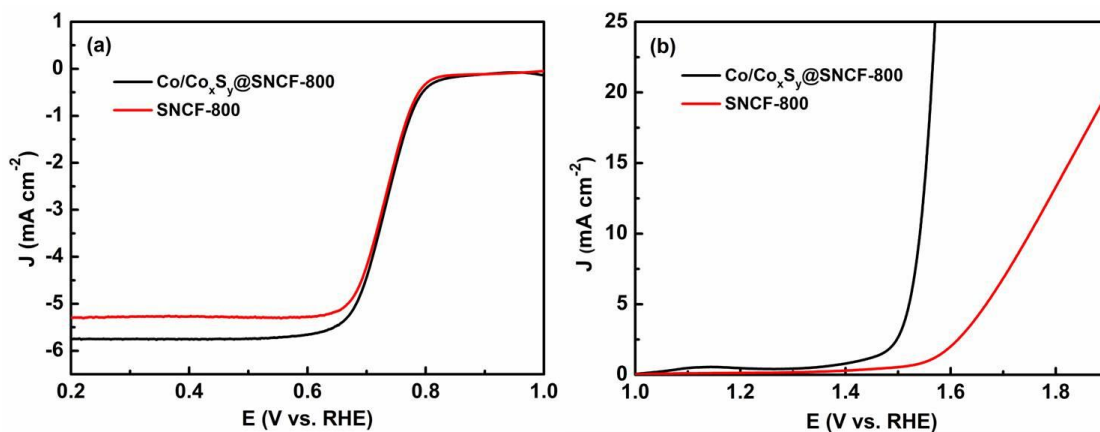


Figure S20. LSV curves of electrocatalysts of Co/Co_xS_y@SNCF-800, SNCF-800 for (a) ORR and (b) OER measurements.

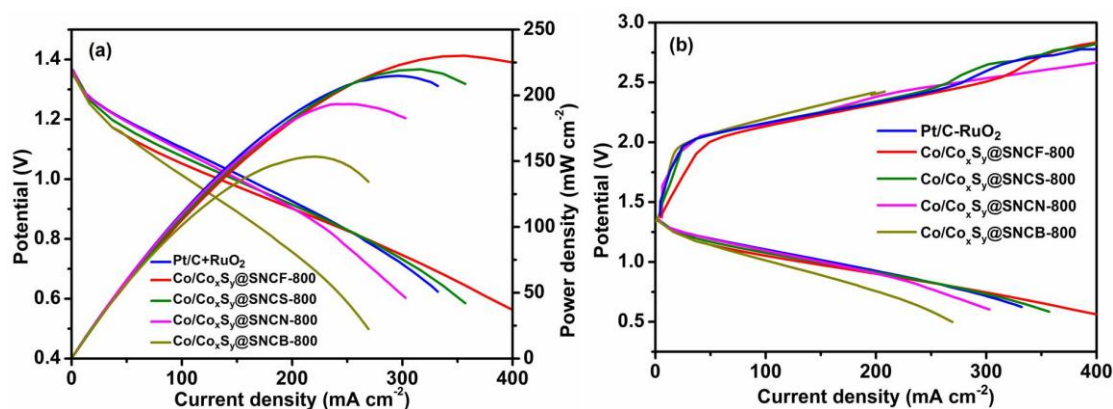


Figure S21. (a) Polarization and power density curves of the primary Zn-air batteries with Co/Co_xS_y@SNCS-800, Co/Co_xS_y@SNCB-800, Co/Co_xS_y@SNCN-800, Co/Co_xS_y@SNCF-800 and Pt/C+RuO₂ catalyst; (b) Charge and discharge polarization curves of Zn-air batteries using Co/Co_xS_y@SNCS-800, Co/Co_xS_y@SNCB-800, Co/Co_xS_y@SNCN-800, Co/Co_xS_y@SNCF-800 and Pt/C+RuO₂ catalyst.